CHEMISTRY OF MATERIALS
Cite This: Chem. Mater. 2019, 31, 3917−3928
Article
pubs.acs.org/cm

Sodium Doping-Enhanced Emission Efficiency and Stability of $CsPbBr_3$ Nanocrystals for White Light-Emitting Devices

Sen Li,[†] Zhifeng Shi,*[,†,‡] Fei Zhang,[†] Lintao Wang,[†] Zhuangzhuang Ma,[†] Dongwen Yang,*[,†] Zhiqiang Yao,[§] Di Wu,[†] Ting-Ting Xu,[†] Yongtao Tian,[†] Yuantao Zhang,[∥] Chongxin Shan,[†,‡,⊥] and Xin Jian Li*[,†,‡]

[†]Department of Physics and Engineering and [§]School of Materials Science and Engineering, Zhengzhou University, Kexue Road 100, Zhengzhou 450001, China

[‡]Key Laboratory of Materials Physics of Ministry of Education, Zhengzhou University, Daxue Road 75, Zhengzhou 450052, China

[∥]State Key Laboratory on Integrated Optoelectronics, College of Electronic Science and Engineering, Jilin University, Qianjin Street 2699, Changchun 130012, China

[⊥]State Key Laboratory of Luminescence and Applications, Changchun Institute of Optics, Fine Mechanics and Physics, Chinese Academy of Sciences, Changchun 130033, China

Supporting Information

ABSTRACT: In this work, an effective strategy through doping of univalent Na^+ ions, which are stable against oxidation and reduction, was proposed to enhance the emission efficiency and stability of orthorhombic $CsPbBr_3$ nanocrystals (NCs). Compared with the fresh $CsPbBr_3$ NCs, a better color purity and a higher photoluminescence quantum yield were achieved, accompanied with a gradual blue shift of the emission peak with an increasing Na^+ doping ratio. On the one hand, the passivation effect with Na^+ doping substantially reduces the nonradiative trap centers in NCs. On the other hand, the density functional theory calculations indicate that the doping of Na^+ ions forms the energetically preferred substitution Na_{Pb}, which increases the optical band gap of $CsPbBr_3$ and the diffusion barrier of Br vacancy in $CsPbBr_3$ structures. Experimentally, the as-synthesized Na^+-doped $CsPbBr_3$ NCs present obvious enhancements in stability against ultraviolet light, heat, and moisture. The above advantages allow us to use such $CsPbBr_3$:Na NCs as solid-state phosphors for white light-emitting device (WLED) applications. Finally, the prepared WLED exhibits a pure white light with Commission International de l'Eclairage color coordinates at (0.31, 0.33), with a color temperature of 6652 K, a color rendering index of 75.2, and a high power efficiency of 67.3 l m/W. More importantly, the WLED shows only 15% decay after continuous runs for as long as 500 h, which demonstrates a great superiority to the reference device with the fresh $CsPbBr_3$ NCs as the phosphors. The approach used here provides an effective strategy to improve the emission efficiency and stability of perovskite NCs, showing promising potentials for their applications in lighting and display fields.

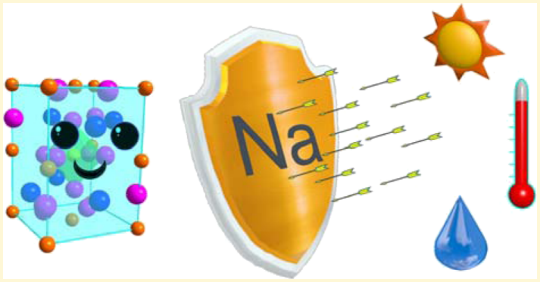

INTRODUCTION

Metal halide perovskites with a chemical formula of ABX_3 (A = CH_3NH_3, $HC(NH_2)_2$, or Cs; B = Pb, Sn, or Ge; X = Cl, Br, or I) have been studied for more than 70 years,[1−6] and they have been in the concern once more after their initial application in photovoltaic cells by Kojima et al. in 2009.[7] Besides the application in photovoltaic cells,[8−11] perovskite materials have exhibited superior performance in other electronic and optoelectronic devices, such as light-emitting diodes (LEDs),[12−15] photodetectors,[16−19] and lasers.[20−22] More recently, inorganic halide perovskite nanocrystals (NCs) have become new research hotspots because of their high photoluminescence quantum yield (PLQY), tunable emission wavelength, high color purity, and simple processing techniques,[23−28] demonstrating great application potentials in the fields of low-cost light sources,[29,30] visible light communication,[31] and displays.[32] In particular, as down-conversion phosphors in display applications, $CsPbX_3$ NCs with red, green, and blue colors show a very wide color gamut, which is 40% more than that of the National Television Standard Committee color standards.[25,33]

However, numerous efforts have been paid and continual innovations have been achieved in the perovskite material processing approaches and device fabrication techniques. On the one hand, the stability of perovskite NCs remains highly unsatisfactory and needs to be improved, which is the main obstacle that hinders the reliable device operation.[34−42] On the other hand, the PLQY of perovskite NCs has to be promoted

Received: December 31, 2018
Revised: May 9, 2019
Published: May 10, 2019

DOI: 10.1021/acs.chemmater.8b05362
Chem. Mater. 2019, 31, 3917−3928

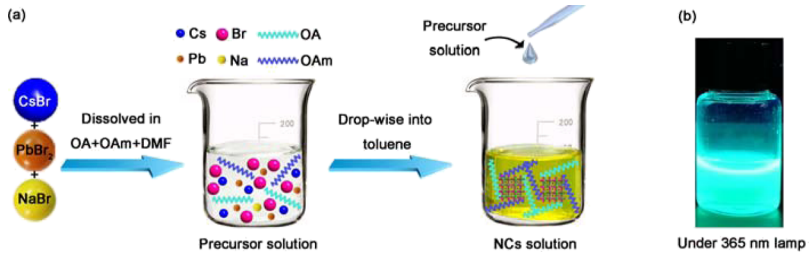

Figure 1. (a) Schematic diagram of the synthesis procedures of the Na^+-doped orthorhombic $CsPbBr_3$ NCs. (b) Photograph of the orthorhombic $CsPbBr_3$:Na NCs in toluene solution under an irradiation of a 365 nm UV lamp.

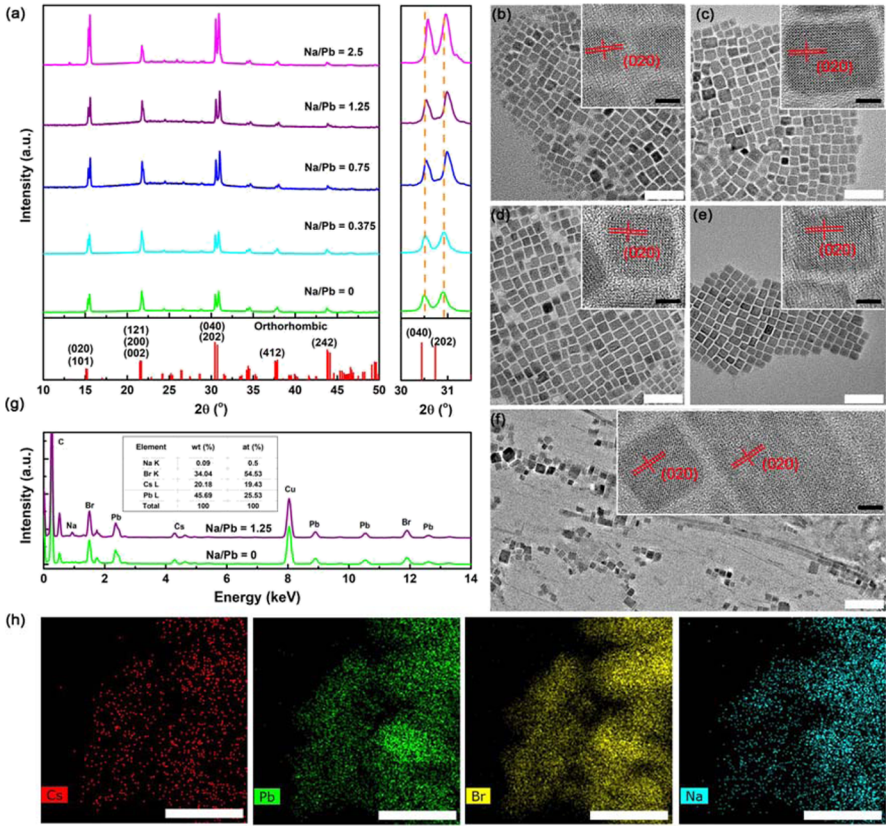

Figure 2. (a) Experimental XRD (left) and the local magnification the (040) and (202) peaks (right) of the $CsPbBr_3$:Na NCs with different Na/Pb ratios and the standard XRD pattern for the orthorhombic phase of $CsPbBr_3$. (b–f) TEM images of the $CsPbBr_3$:Na NCs with different Na/Pb ratios. The white scale bar is 50 nm. The insets in the top right corners show the corresponding high-resolution TEM images. The black scale bar is 5 nm. (g) EDS spectra of the $CsPbBr_3$ (Na/Pb = 0) and $CsPbBr_3$:Na NCs (Na/Pb = 1.25). The inset table shows the element ratio in $CsPbBr_3$:Na NCs (Na/Pb = 1.25). (h) EDS mapping of $CsPbBr_3$:Na NCs (Na/Pb = 1.25). The white scale bar is 30 nm.

further for device fabrication. Therefore, from application point of view, there are still many remaining obstacles or potential breakthroughs for perovskite NCs. To enhance the stability and fluorescence of the perovskite NCs, a few effective ways, such as surface coating and inner doping of the NCs, have been proposed. For surface coating, insulating oxides (such as silica oxide, titanium oxide, and alumina) or polymers [such as poly(methyl methacrylate), polydimethylsiloxane] are often used as barrier materials to protect the NCs from oxidation, moisture, and other chemical attack.[43−46]

However, such coating layers usually make it unfavorable in device manufacture. In comparison, the strategy of doping, intentionally introducing heteroatoms into a target lattice, holds great promise in modulating the material properties of semiconductors. Many kinds of metal ions (including Bi^{3+}, Al^{3+}, Cu^{2+}, Mn^{2+}, Sn^{2+}, Cd^{2+}, and Zn^{2+}) and rare-earth ions (e.g., Eu^{3+}, Ce^{3+}, Yb^{3+}, and Tb^{3+}) have been introduced into halide perovskites to replace Pb^{2+} or Cs^+ ions to reduce the defect state density, passivate grain boundaries, improve PLQY, or enhance the stability of perovskites.[47−60] Lately, interstitial doping of alkali metal cations into the lattice of a perovskite film have been focused on. For example, Liu et al. found that the addition of K^+ ions clearly improved the quality of a perovskite film by enlarging the grain sizes, reducing the defect state density, and passivating the grain boundaries, which finally push the performance of the planar perovskite solar cells to a higher level.[61] Cao et al. incorporated extrinsic alkali cations (Li^+, Na^+, K^+, and Rb^+) in a triple cation perovskite film, and they considered that the alkali cations occupied the interstitial sites of the perovskite lattice, and consequently the hysteresis of cells was reduced owing to the increase of ion migration barriers.[62] Theoretical studies of Son

DOI: 10.1021/acs.chemmater.8b05362
Chem. Mater. 2019, 31, 3917−3928

et al. suggested that K^+ energetically preferred the interstitial site and was able to prevent the formation of iodide Frenkel defects and resolve the hysteresis in perovskite solar cells.[63] Tang's group doped an inorganic $CsPbBr_3$ perovskite film with various alkali metal cations, which promoted the crystallized dynamics, electrical energy distribution, and radiative recombination.[64] The PLQY of the $CsPbCl_3$ quantum dots (QDs) was enhanced from 3.2 to 10.3% by the doping of potassium ions (K^+) by Song's group.[57] However, in most studies, the alkali metal cations were usually considered to form interstitial sites in the targets, just considering that the ionic size of the alkali metal cations is much smaller than that of Cs^+, without a clear demonstration of the inherent doping mechanism. What's more, the doping of Na^+ cations in zero-dimensional $CsPbBr_3$ NCs for adjusting the optical properties remains untouched as far as we know.

We adopt a facile and effective approach to improve the emission efficiency and stability of orthorhombic $CsPbBr_3$ NCs by an in situ doping of univalent Na^+ ions during the supersaturated solution recrystallization process at room temperature (RT). In addition to an enhanced PLQY, a better color purity and the blue shift phenomenon of the emission peaks can be observed for the Na^+-doped $CsPbBr_3$ NCs. Density functional theory (DFT) calculations show that the doping of Na^+ ions forms the energetically preferred substitution Na_{Pb} doping, which increases the optical band gap (E_g) of $CsPbBr_3$ and the diffusion barrier of Br vacancy (V_{Br}^+) in the orthorhombic $CsPbBr_3$ structures. Compared with the fresh $CsPbBr_3$ NCs, a substantially improved material stability against ultraviolet (UV) light, heat, and environmental oxygen/moisture was achieved. Further, the obtained orthorhombic $CsPbBr_3$:Na NCs were employed as the solid-state phosphors in white light-emitting device (WLED) fabrication, producing a color temperature (CCT) of 6652 K, a color rendering index (CRI) of 75.2, and Commission Internationale de L'Eclairage (CIE) color coordinates of (0.31, 0.33) 67.3 l m/W. Moreover, the proposed WLEDs in a continuous current mode demonstrate a remarkable long-term stability even when operated in ambient air, and only ∼15% emission decay appears after 500 h of running time, greatly superior to the reference device with the fresh orthorhombic $CsPbBr_3$ NCs as the phosphors. The outstanding performances and facile method used here will make such orthorhombic $CsPbBr_3$:Na NCs attractive for applications in optoelectronics and industrial fields.

RESULTS AND DISCUSSION

In the experiment, a supersaturated recrystallization method was used to synthesize Na^+-doped $CsPbBr_3$ NCs. The synthesis procedures are illustrated in Figure 1a, and the detailed process can be found in the Experimental Section. In our case, five samples with different nominal doping concentrations of 0, 0.375:1, 0.75:1, 1.25:1, and 2.5:1 for Na/Pb ratios were synthesized by just changing the amount of NaBr in the precursors. We first investigated the influence of Na^+ doping concentration on the structural properties of $CsPbBr_3$:Na NCs by X-ray diffraction (XRD) and transmission electron microscopy (TEM) measurements. As shown in Figure 2a, the $CsPbBr_3$ NCs irrespective of doping or not are characterized by the orthorhombic phase (a = 8.24 Å, b = 8.20 Å, c = 11.74 Å), which can be well-discriminated by the split of diffraction peaks at ∼31.0° (Figure S1, Supporting Information), also indicating that the Na^+ doping does not affect the crystalline structure of the $CsPbBr_3$ hosts. Such structural characteristics are similar to the observations in previous studies where the $CsPbBr_3$ QDs were also synthesized at RT.[23,65] The local magnification the (040) and (202) peaks of the XRD patterns shows a gradual peak shift toward higher angles, which may be caused by the substitution of Pb^{2+} with smaller Na^+ cations to result in lattice contraction. This is similar to the previous reports using potassium and lanthanide as the doping ions.[57,64] In the studies, the XRD patterns gradually shift toward the large angle side, and it was believed to be caused by the substitution of Cs^+ by smaller alkali metal cations in the cubic perovskite lattice.

Also, the XPS survey spectra and high-resolution spectra involving Na 1s, Pb 4f, and Br 3d were measured to further detail the existence of Na dopant in the host NCs and their electronic states. As shown in Figure S2 (Supporting Information), the spectra of the Pb $4f_{5/2}$ and $4f_{7/2}$ peaks and Br $3d_{3/2}$ and $3d_{5/2}$ peaks have shifted to higher binding energies, indicating the modified chemical environment after Na incorporation, which confirms that Na is effectively doped in the NCs. However, as the Na/Pb ratio increases to 2.5, the native diffraction signals decay sharply, and the diffraction peak located at ∼15.0° increases markedly, which presumably results from the oriented growth of the material along the [020] direction.

Figure 2b−e exhibits the typical TEM images of the $CsPbBr_3$:Na NCs, from which some distinct and regular trends were revealed. First, the shape of $CsPbBr_3$:Na NCs was preserved at a low doping level (Na/Pb ≤ 1.25) and the dispersion of NCs is almost unaffected, and a well-defined crystalline structure can be observed from the high-resolution TEM images shown in the insets. However, as shown in Figure 2f, when the Na/Pb ratio reaches 2.5, some of the NCs grow into long nanowires with micrometer-scale length and nanometer-scale width, which might explain the increase of the diffraction peak at ∼15.0° from the corresponding XRD pattern shown above.

Also, such nanowires are still characterized by the single-crystallinity properties. Second, together with the size distribution statistics in Figure S3 (Supporting Information), it can be seen that the uniformity of size distribution for $CsPbBr_3$:Na NCs was improved gradually as the Na/Pb ratio increases from 0 to 1.25; thus, an improved emission purity for the photoluminescence (PL) spectra obtained can be understandable. To verify the incorporation of guest Na^+ cations, we investigated the chemical composition of the $CsPbBr_3$:Na NCs (Na/Pb = 1.25) by the energy-dispersive X-ray spectroscopy (EDS) measurements, and the data from fresh $CsPbBr_3$ NCs were also measured and put together for comparison. In addition to the elements of Cs, Pb, and Br, Na is also identified in the $CsPbBr_3$:Na NCs, as shown in Figure 2g. Moreover, the quantitative analysis of the EDS spectrum gives a quantified atom ratio (%) of 19.43:25.53:54.53:0.5 for Cs/Pb/Br/Na. A relatively high Na volume indicates that Na^+ cations were effectively doped in the hosts of $CsPbBr_3$ NCs. The EDS and XPS survey spectra of $CsPbBr_3$:Na NCs with different Na/Pb ratios were measured to identify the exact doping amount in the Cs/Pb/Br/Na NCs (Figures S4 and S5 and Table S1 in Supporting Information). The results confirm that Na doping is effective in all Na/Pb ratios, and the real doping amount increases with the nominal doping amount. Further analysis of the EDS elemental mapping of the $CsPbBr_3$:Na NC samples is performed by employing Cs, Pb, Br, and Na as the target

DOI: 10.1021/acs.chemmater.8b05362
Chem. Mater. 2019, 31, 3917−3928

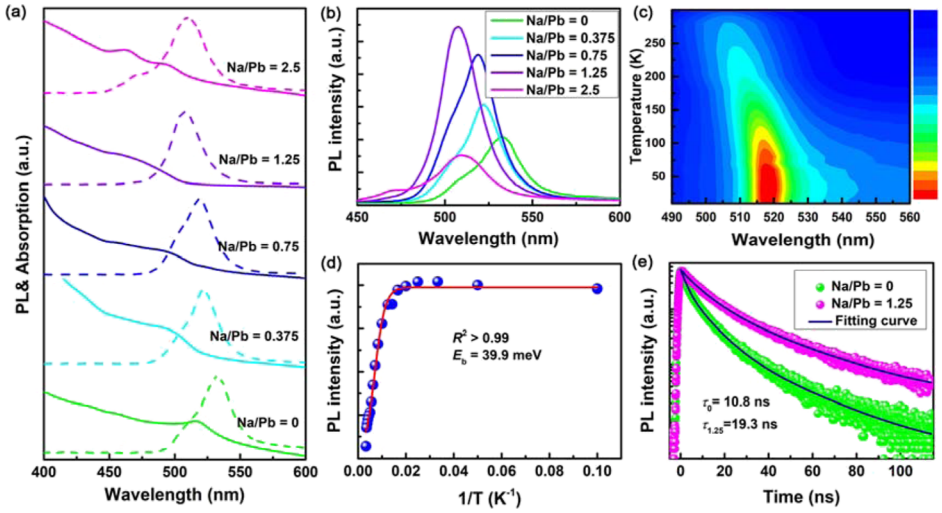

Figure 3. (a) PL and optical absorption spectra of the $CsPbBr_3$:Na NCs with different Na/Pb atom ratios. (b) PL spectra of the samples with different Na/Pb atom ratios, showing the variation of peak position and fwhm. (c) Pseudocolor map of temperature-dependent PL spectra of the $CsPbBr_3$:Na NCs (Na/Pb = 1.25) taken from 10 to 300 K. (d) Integrated PL intensity of the $CsPbBr_3$:Na NCs with the Na/Pb ratio of 1.25 as a function of temperature. (e) PL decay spectra and the fitting curves of two typical $CsPbBr_3$:Na NCs with the Na/Pb ratio of 0 and 1.25.

elements. As shown in Figure 2h, four target elements are uniformly distributed throughout the entire selected area, confirming the effective synthesis of $CsPbBr_3$:Na NCs and the uniform doping of Na^+ in them.

Further, the optical absorption and steady-state PL spectra of the colloidal $CsPbBr_3$:Na NCs with different Na/Pb atom ratios were measured and summarized in Figure 3a. One can clearly see that the absorption edge of the $CsPbBr_3$:Na NCs shifted gradually to the high-energy side with an increasing dopant Na^+ content, indicating a slight regulation of the band gap of the $CsPbBr_3$ NCs by Na^+ doping. Correspondingly, the position of the emission peaks displays a regular blue shift trend. An additional observation is that there is a small Stokes shift by 10−20 nm between the absorption edge and the corresponding emission peak, implying that the PL emission of the $CsPbBr_3$:Na NCs originates from the direct exciton recombination.[26] For a more detailed comparison, the PL spectra of the $CsPbBr_3$:Na NCs with different nominal Na/Pb ratios were put together in Figure 3b. It can be seen that with the increase of NaBr concentration, in the range of 0.375−1.25 for Na/Pb ratio, the PL intensity of the NCs enhances enormously; meanwhile, the PL curves become more narrow and symmetric. At a Na/Pb ratio of 1.25, the maximum emission intensity was achieved with a rather high PLQY of 85%, nearly 2 times larger than that of fresh $CsPbBr_3$ NCs (~44%, Figure S6, Supporting Information). However, when the Na/Pb ratio reaches 2.5, the PL intensity drops severely, and the corresponding PL curve evolves into two peaks. Note that, in our case, all the $CsPbBr_3$:Na NC samples were collected from the as-synthesized products without purification. Hence, the higher PLQY and lower full width at half-maximum (fwhm) for $CsPbBr_3$:Na NCs (Na/Pb = 1.25) ought to originate from the substantially improved crystallinity and size uniformity of NCs. The PL spectra of the $CsPbBr_3$:Na samples after purification are shown in Figure S7 (Supporting Information), which shows that the PL peak position remains unchanged after purification, but the PL spectra are more narrow and symmetric at the same time.

To gain more insights into the optical recombination mechanisms of the $CsPbBr_3$:Na NCs, temperature-dependent PL measurement was performed for a representative sample (Na/Pb = 1.25) within the temperature range of 10−300 K. As shown in Figures 3c and S8a (Supporting Information), obvious changing trends of the luminescence characteristics were revealed. First, the emission intensity of the $CsPbBr_3$:Na NCs decreased gradually with the increase of the temperature, which results from the thermally activated nonradiative recombination. The temperature-dependent PL spectra of $CsPbBr_3$ NCs seem to show a similar variation (Figure S9a, Supporting Information). The overall temperature quenching behavior could be described by the following expression

$$I(T) = \frac{I_0}{1 + A \exp\left(-\frac{E_b}{k_B T}\right)} \quad (1)$$

where I_0 is the PL intensity at 0 K, A is the proportional constant, k_B is the Boltzmann constant, and E_b is the exciton binding energy. As shown in Figure 3d, the fitting curve yields a value of 39.9 meV for E_b, larger than that of fresh $CsPbBr_3$ NCs (35.7 meV, Figure S9b, Supporting Information). In theory, the relatively higher E_b ensures the survival of excitons well above RT and even higher temperatures and also their high-rate recombination; thus, an improved PLQY and a better temperature tolerance of $CsPbBr_3$:Na NCs can be expected.[66−68] Second, a monotonous red shift of emission peak was observed in the temperature range of 300−10 K, and this trend is opposite to the well-known Varshni relation. The electron−phonon renormalization and the crystal lattice thermal expansion were considered to be responsible for the phenomenon, which is similar to that reported in lead/copper chalcogenide semiconductors.[69] Third, no structural phase transition occurs within the cooling process from 300 to 10 K because there is no irregular and reversal PL shift, unlike other reports on the $MAPbBr_3$ and $MAPbI_3$ systems.[70] Fourth, an fwhm broadening behavior of the PL emission peak was observed, and the summarized data were fitted using the independent Boson model to examine the exciton−phonon interaction in the carrier recombination process. Such evolution can be fitted with eq 2[15,27]

DOI: 10.1021/acs.chemmater.8b05362
Chem. Mater. 2019, 31, 3917−3928

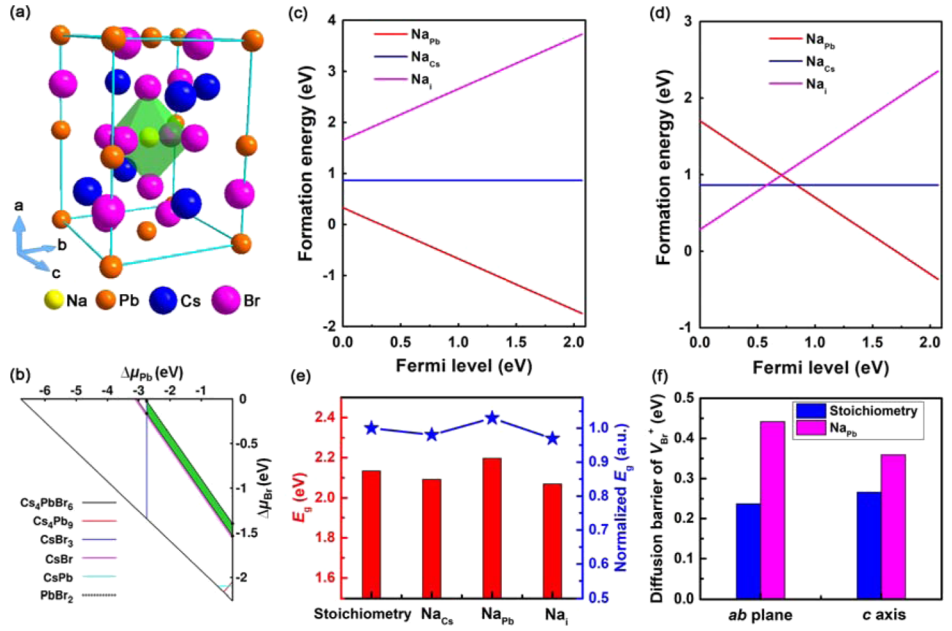

Figure 4. (a) Schematic illustration of Na^+-doped orthorhombic $CsPbBr_3$ structure. (b) Calculated phase stability diagram of $CsPbBr_3$ against $\Delta\mu_{Pb}$ and $\Delta\mu_{Br}$. The green polygon stands for the thermal dynamic stable window, and each line represents one competing phase. We choose the representative points A (μ_{Cs} = −3.53 eV, μ_{Pb} = −2.74 eV, μ_{Br} = −0.16 eV) and B (μ_{Cs} = −2.16 eV, μ_{Pb} = 0 eV, μ_{Br} = −1.53 eV) for the formation energy study. (c,d) Formation energies of intrinsic point defects (i.e., Na_{Pb}, Na_{Cs}, and Na_i) as a function of Fermi level using the chemical potentials corresponding to points A and B in the phase diagram of $CsPbBr_3$. (e) Calculated band gap E_g and normalized E_g of the $CsPbBr_3$ structure with and without defects. (f) Calculated diffusion barrier of V_{Br}^+ for diffusion paths on the *ab* plane and along the *c* axis.

$$\Gamma(T) = \Gamma_0 + \sigma T + \frac{\Gamma_{OP}}{\exp(\hbar\omega_{OP}/KT) - 1} \quad (2)$$

where the first, second, and third parts correspond to inhomogeneous broadening, exciton−acoustic phonon, and exciton−optical phonon interactions, respectively, and $\hbar\omega_{op}$ is the optical phonon energy. We can observe that Γ_0 dominates $\Gamma(T)$ at low temperatures, and at higher temperatures, the contributions from acoustic and optical phonons are larger than Γ_0, which ultimately leads to a nonlinear increase of fwhm.

As presented in Figure S8b (Supporting Information), a value of 27.7 meV for $\hbar\omega_{op}$ was derived, slightly larger than that of fresh $CsPbBr_3$ NCs (24.1 meV, Figure S9c, Supporting Information). Therefore, after Na^+ doping, the optical phonon energy of $CsPbBr_3$ NCs increases. The relatively stronger exciton−phonon interaction of the $CsPbBr_3$:Na NCs suggests the enhanced and desirable thermal antiquenching effects required at high temperatures. Thus, the $CsPbBr_3$:Na NCs can be expected to operate with a better stability.

To further understand the exciton recombination dynamics of the $CsPbBr_3$:Na NCs (Na/Pb = 1.25), time-resolved PL measurements were performed, and the data from the fresh $CsPbBr_3$ NCs were also measured and put together for comparison. As shown in Figure 3e, the average PL lifetime for $CsPbBr_3$:Na NCs was measured to be 19.3 ns, which was longer than that of the fresh $CsPbBr_3$ QD counterparts (10.8 ns). Herein, we consider that the lengthening of the PL lifetime after Na^+ doping may be caused by the decrease of the charge carrier trapping states, manifesting the positive role of Na^+ ions in the lattice of $CsPbBr_3$ NCs; thus, the efficient usage of excited carriers is favored, resulting in a higher PLQY and a long PL lifetime. Further, we estimated the radiative (k_r) and nonradiative (k_{nr}) rate constants of the two samples based on the obtained PLQY and average PL lifetime.[24] As summarized in Table S2 (Supporting Information), the k_{nr} value of the $CsPbBr_3$:Na NCs drops by a factor of ∼50 compard with the fresh $CsPbBr_3$ NCs, explaining the higher PLQY of $CsPbBr_3$ NCs after Na^+ doping.

To confirm the occupancy site of the Na^+ ion in the perovskite site, we subsequently investigated the energetics by using DFT calculations. A schematic illustration of Na^+-doped orthorhombic $CsPbBr_3$ structure is shown in Figure 4a. In the thermodynamic equilibrium growth conditions, the existence of $CsPbBr_3$ should satisfy eqs 3−5

$$\Delta\mu_{Cs} + \Delta\mu_{Pb} + 3\Delta\mu_{Br} = \Delta H_{CsPbBr_3} \quad (3)$$

$$\Delta\mu_i \le 0 \ (i = \text{Cs},\ \text{Pb},\ \text{Br}) \quad (4)$$

$$h_j\Delta\mu_{Cs} + k_j\Delta\mu_{Pb} + l_j\Delta\mu_{Br} \le \Delta H_{Cs_{h_j}Pb_{k_j}Br_{l_j}}, \qquad j = 1\cdots Z \quad (5)$$

where $\Delta\mu_i$ is the chemical potential of the constituent element referred to its most stable phase. Equation 3 is for thermodynamic equilibrium; eq 4 is to prevent the atomic species from precipitating to elemental phases; and eq 5 is to avoid the formation of any secondary competing phase. The chemical potentials of Pb and Br satisfying eqs 3−5 are shown as the green region in Figure 4b. One can see that the stable region is narrow, which manifests poor long-term stability of the $CsPbBr_3$ structure under ambient conditions. In the present case, three possible point defects were considered, including Na_{Pb}, Na_{Cs}, and Na_i. As the chemical potential of the constituent elements decide the formation energies of point defects, we herein choose two representative points, A (Pb-poor) and B (Pb-rich), in the chemical range (Figure 4b). The formation energies of Na_{Pb}, Na_{Cs}, and Na_i as a function of Fermi level at the chemical potentials of A and B are shown in

DOI: 10.1021/acs.chemmater.8b05362
Chem. Mater. 2019, 31, 3917−3928

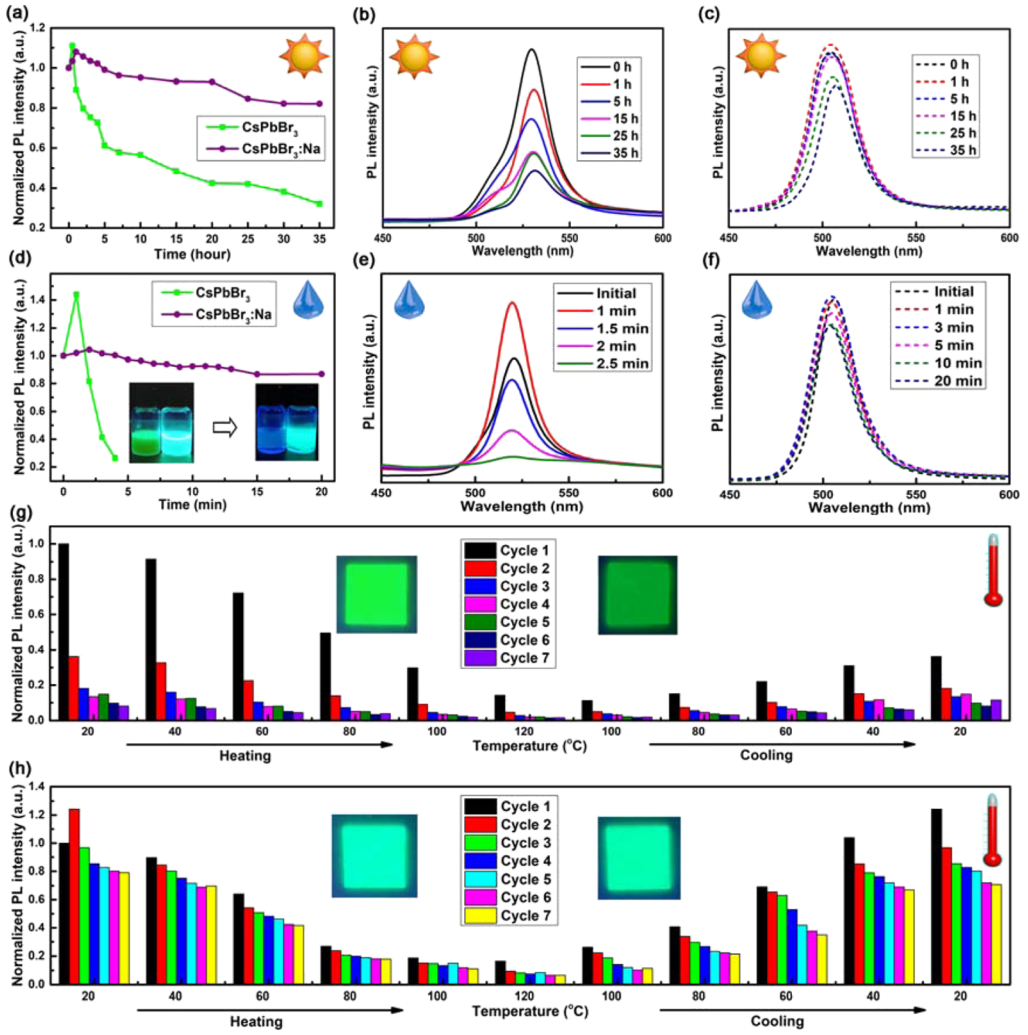

Figure 5. (a) Normalized PL intensity of the fresh $CsPbBr_3$ and $CsPbBr_3$:Na (Na/Pb = 1.25) NCs under continuous UV light radiation (365 nm, 20 W). (b,c) PL spectra of the fresh $CsPbBr_3$ and $CsPbBr_3$:Na NCs recorded at different time intervals. (d) Normalized PL intensity of the fresh $CsPbBr_3$ and $CsPbBr_3$:Na (Na/Pb = 1.25) NCs after adding 10% volume ratio of deionized water into the NC solution. The insets show the photographs of two samples (left, $CsPbBr_3$ NCs; right, $CsPbBr_3$:Na NCs) under UV light irradiation before and after moisture testing. (e,f) PL spectra of the fresh $CsPbBr_3$ and $CsPbBr_3$:Na (Na/Pb = 1.25) NCs recorded at different time intervals after adding deionized water. The thermal stability of (g) fresh $CsPbBr_3$ NCs and (h) $CsPbBr_3$:Na NCs in seven thermal cycling measurements are shown. The insets show the photographs of the two samples under UV light irradiation before and after the seven thermal cycling measurements.

Figure 4c,d. According to the previous formation energy calculations of native defects, the Fermi level would be pinned close to the valence band maximum (VBM) at Pb-poor conditions and conduction band minimum (CBM) at Pb-rich conditions.[71,72] As shown in Figure 4c, the formation energy of the Na_{Pb} defect is the lowest, regardless of the position of the Fermi level. Moreover, when the Fermi level is close to CBM, the formation energy of the Na_{Pb} defect is still the lowest among all defects. The formation energy calculation demonstrates that Na_{Pb} is the dominant defect in the Na^+-doped orthorhombic $CsPbBr_3$ structure. We further investigated the band gaps of the defect-free and defect structures with Na_{Pb}, Na_{Cs}, and Na_i. In comparison with the defect-free structure, the band gap of $CsPbBr_3$ with the Na_{Pb} defect increases (Figure 4e), which is also consistent with the blue shift in the experimental observation. We also extended the theoretical investigation into the migration of native defects (i.e., V_{Br}^+). As shown in Figure 4f, the formation of the Na_{Pb} defect with Na ion incorporation leads to substantial increases of the diffusion barrier of V_{Br}^+ in the diffusion paths along the *ab* plane and *c* axis. Thus, the nondiffusion of intrinsic defects would also increase the chemical stability of the Na^+-doped $CsPbBr_3$. It is well-known that the stability of halide perovskites has always been criticized, which has been the main obstacle hindering their potential applications significantly. To assess the suitability of the as-synthesized $CsPbBr_3$:Na NCs to practical optoelectronic device applications, we investigated the environmental stability of the products in detail by analyzing the effects of UV light irradiation, water, and heat on the optical properties of $CsPbBr_3$:Na NCs. Experimentally, a portable UV lamp with a power density of 4 mW/cm^2 was used as the irradiation source to investigate the photostability of the products. As shown in Figure 5a, after a continuous irradiation for 35 h, the fresh $CsPbBr_3$ NCs experience a rapid fluorescence quenching, retaining only 30% of the original intensity. In sharp contrast, the $CsPbBr_3$:Na NCs maintain above 80% of the initial PL performance even within the same irradiation period, demonstrating a substantially enhanced photostability. Figure 5b,c presents the corresponding PL spectra of the $CsPbBr_3$ and $CsPbBr_3$:Na NCs recorded at

DOI: 10.1021/acs.chemmater.8b05362
Chem. Mater. 2019, 31, 3917−3928

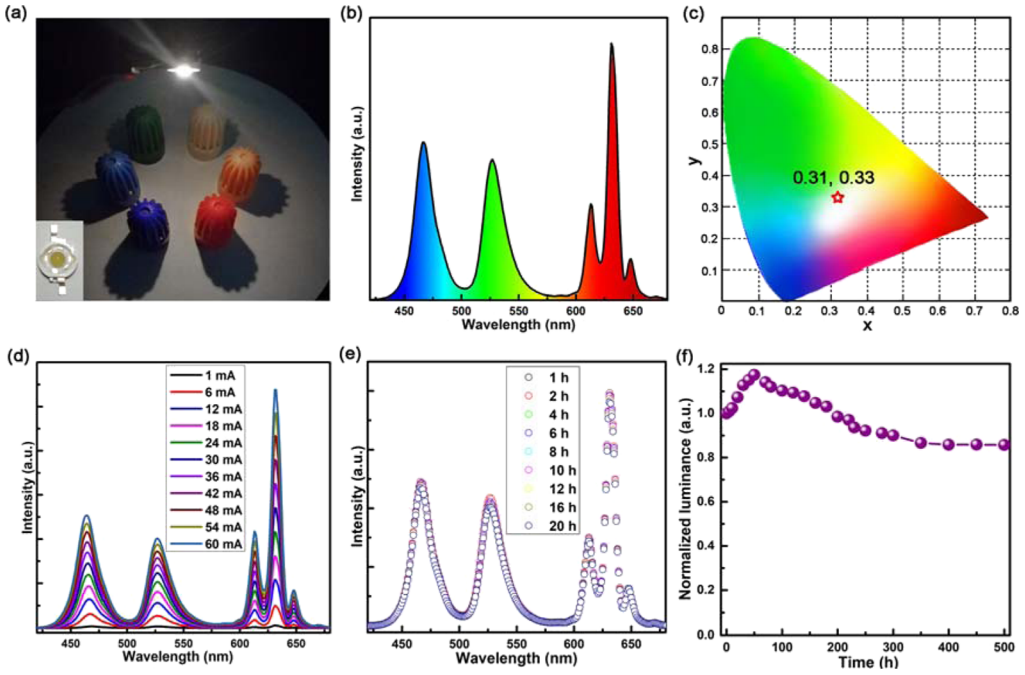

Figure 6. (a) Photographs and (b) typical emission spectra of the $CsPbBr_3$:Na WLED operated at 9 mA. (c) CIE color coordinates of the WLED plotted on the CIE1931 color space chromaticity chart. (d) Emission spectra of the WLED at different driving currents ranging from 1 to 60 mA. (e) Emission spectra of the WLED after different running periods under the same bias and measurement conditions. (f) Normalized luminance of the WLED measured for a continuous operation for 500 h.

different time intervals. One can also observe that the $CsPbBr_3$:Na NCs are much more stable than the $CsPbBr_3$ NCs against UV light irradiation. Besides, the spectral shapes of the two samples recorded at different time intervals remain unchanged. Unexpectedly, yet interesting, a PL intensity enhancement for $CsPbBr_3$ and $CsPbBr_3$:Na NCs was observed in the initial stage of UV light illumination, which is presumably because of the photoinduced regrowth of NCs.[73,74] Then, the PL intensity of the $CsPbBr_3$ NCs decreases rapidly with time, and the intensity dropped to only about 30% of the initial intensity after 35 h. In comparison, the $CsPbBr_3$:Na NCs are much more stable against UV light, and the PL intensity decreases only 15% in the same time.

To study the moisture stability of the as-synthesized $CsPbBr_3$:Na NCs, a 10% volume ratio of deionized water was injected into the $CsPbBr_3$ NC solution (concentration: 0.2 mg/mL in toluene), and a quantitative study has been carried out by monitoring the PL evolution with time. For comparison, the same measurement was also conducted on the fresh $CsPbBr_3$ NCs with the same concentration as that of the $CsPbBr_3$ NC solution, and the obtained results are put together in Figure 5d. One interesting phenomenon that deserves comment is that a significant increase (~40%) in the PL intensity for $CsPbBr_3$ NCs can be identified in the initial 1 min. We consider that such PL enhancement is closely related with the appearance of the hydrolysis product, which formed on the surface of the $CsPbBr_3$ NCs and passivated the undesirable surface defects, thus making the enhancement of PL emission possible. Unfortunately, such a phenomenon fades away very quickly, and only ~20% of the remnants are left after the 2.5 min test. However, for Na^+-doped $CsPbBr_3$ NCs, the fluorescence quenching is relatively slow, retaining more than 85% of the initial performance even with a longer test period. The insets in Figure 5d display the corresponding photographs of fresh $CsPbBr_3$ NCs (left) and $CsPbBr_3$:Na NCs (right) under UV light irradiation before and after the moisture testing. Although a slight weakening of the emission intensity can be identified for the $CsPbBr_3$:Na NCs, the sample still has a strong fluorescence. In comparison, the fresh $CsPbBr_3$ NCs lost most of the brightness after only 2.5 min of the test, gradually changing from green to colorless. Figure 5e,f displays the corresponding PL spectra of the fresh $CsPbBr_3$ and $CsPbBr_3$:Na NCs recorded at different time intervals after adding deionized water, matching well with the above observations.

To compare the thermal stability of the $CsPbBr_3$ NCs before and after Na^+ doping, thermal cycling measurements were performed by heating the sample from 20 to 120 °C, and then cooling from 120 to 20 °C, and so on. Here, under atmosphere conditions, the films made by dropping the NCs onto a glass substrate were heated to as high as 120 °C and then cooled down to RT, and the integrated PL intensity of the two samples at all temperature points was plotted. As shown in Figures 5g and S10 (Supporting Information), we can see that the PL intensity of the fresh $CsPbBr_3$ NCs gradually reduces when temperature (heating process) increases. When the cooling process was finished, a substantial emission decay of about 60% occurs. The emission intensity is unrecoverable, which implies an undesirable thermal degradation of PL performance, and the generation of additional nonradiative recombination centers at high temperature should be responsible for this phenomenon. Continuous emission dropping lasts in the next six heating/cooling cycles, and consequently the PL intensity decreases to only about 10% of the initial value. The insets in Figure 5g display the corresponding photographs of the $CsPbBr_3$ NC samples under UV light irradiation before and after seven thermal cycling measurements, and an obvious weakening in green emission can be distinguished. In contrast, the emission

DOI: 10.1021/acs.chemmater.8b05362
Chem. Mater. 2019, 31, 3917−3928

performance from the $CsPbBr_3$:Na NCs differs sharply. As shown in Figures 5h and S10 (Supporting Information), after the first heating/cooling cycle, an unexpected emission enhancement by ~25% was produced compared with the original emission intensity, which is totally different from the case of fresh $CsPbBr_3$ NCs. Obviously, such phenomenon manifests the critical role of Na^+ doping in enhancing the thermal stability of $CsPbBr_3$ NCs. We herein consider that the enhanced emission in $CsPbBr_3$:Na NCs after the thermal cycling measurement is conceivable because excess Na^+ dopants beyond the optimal doping concentration could be excluded from the $CsPbBr_3$ NC host if they were exposed to high temperature condition, producing the most thermodynamically stable NCs. However, successive heating/cooling cycles would still induce emission decay although the decay magnitude is very small. Finally, the emission intensity of the $CsPbBr_3$:Na NCs was maintained at about 80% of the initial value after the seven heating/cooling cycles, much better than those of the undoped counterparts. The above experimental results indicate a substantially improved thermal stability for the Na^+-doped $CsPbBr_3$ NCs, thus opening up enormous opportunities for obtaining high-performance optoelectronic devices with good temperature tolerance. The stability of $CsPbBr_3$:Na NCs with different Na/Pb ratios against UV light, moisture, and heat was also tested, and the results are shown in Figure S11 (Supporting Information). It is clear that the doping of Na surely enhances the stability of NCs. What's more, $CsPbBr_3$:Na NCs with the Na/Pb ratio of 1.25 have the best stability. Besides, the improved storage stability of the Na^+-doped $CsPbBr_3$ NCs was confirmed by monitoring the evolution of their optical and structural properties with time. As shown in Figure S12 (Supporting Information), the initial PL performance of the $CsPbBr_3$:Na NCs can almost be maintained after 6-day storage in ambient air, whereas the emission decay for the fresh $CsPbBr_3$ NC counterparts is very significant over the same measurement period. Figure S13 (Supporting Information) displays the XRD patterns of the $CsPbBr_3$ and $CsPbBr_3$:Na NCs at different times. One can see that the $CsPbBr_3$:Na NCs possess a good environment stability against water/oxygen degradation, which preserves the structural integrity after 30-day storage in ambient conditions. By comparison, for the undoped counterpart, the impurity phase appears after 30 days. Such remarkable material stability together with the good emission performance provide unequivocal evidences of the positive role of the Na^+ dopant, and the reliable $CsPbBr_3$:Na NCs compatible for practical applications under harsh conditions are also evident.

To demonstrate the potential application of $CsPbBr_3$:Na NCs as phosphors in lighting technology, a WLED was designed and fabricated by simply combining these green-emissive $CsPbBr_3$:Na NCs and the red-emissive $K_2SiF_6:Mn^{4+}$ (KSF) powder above a blue-emissive LED chip (470 nm), considering that both green $CsPbBr_3$:Na NCs and red KSF have excitations in the blue light region. The working WLED in Figure 6a (driving current: 9 mA) exhibits a bright white light with good color discrimination. Figure 6b displays the typical emission spectra of the WLED operated at 9 mA, and three discrete emission peaks located at 447, 509, and 700 nm can be identified, which correspond respectively to the emission contributions from the blue LED chip, green $CsPbBr_3$:Na NCs, and red KSF phosphors (Figure S14, Supporting Information). Figure 6c presents the CIE color coordinates of the device, which was measured with the coordinates of (0.31, 0.33), falling in the white-light region and providing the possibility for backlight utilization. Besides, the CCT and CRI of the WLED were measured to be 6652 K and 75.2 with a high power efficiency of 67.3 l m/W. The emission spectra of the WLED as a function of the driving current are shown in Figure 6d. As the driving current was increased from 1 to 60 mA, three emission components increase simultaneously, and no premature saturation toward the blue light excitation occurs. Correspondingly, there is almost no change in the CIE color coordinates, suggesting that the emission contributions from the two phosphors increase with the driving current in the same proportion, also indicating the good photostability of both phosphors. The above results suggest that the $CsPbBr_3$:Na NCs could function as efficient down-conversion phosphors for WLED fabrication. To further assess the device stability, we monitored the emission spectra of the WLED after different running periods in open air, in which the injection current was fixed at 9 mA. As shown in Figure 6e, after continuous running for 20 h, there is no change in the emission intensity, spectra shape, and the peak position, demonstrating a remarkable long-term operation stability of the WLED constructed with the $CsPbBr_3$:Na NCs. For comparison, a reference WLED constructed with fresh $CsPbBr_3$ NCs was also fabricated and measured (Figure S15, Supporting Information). As shown in Figure S16 (Supporting Information), only within the running test for 10 h, an obvious emission decay for 50% of the green emission component was produced with the red emission component unchanged. The results show that the fresh $CsPbBr_3$ NCs are more fragile to the blue light excitation than $CsPbBr_3$:Na NCs, which are consistent with the photostability results discussed above. At last, a continuous running test of 500 h for the proposed WLED was performed, and only an intensity decay of ~15% was produced, as displayed in Figure 6f. Together with the advantage of improved emission efficiency, the Na^+-doped $CsPbBr_3$ NCs can therefore be deemed as reliable down-conversion phosphors in the application in WLEDs.

CONCLUSIONS

In conclusion, a doping strategy by univalent Na^+ ions was performed to enhance the emission efficiency and stability of orthorhombic $CsPbBr_3$ NCs. Compared with the fresh $CsPbBr_3$ NCs, the emission purity and PLQY were substantially improved, and the blue shift phenomenon was also observed. Moreover, the as-synthesized Na^+-doped $CsPbBr_3$ NCs demonstrate an enhanced stability against UV light, heat, and moisture. The detailed reasons and the doping mechanisms were further analyzed by the temperature-dependent and time-resolved PL measurements and the DFT calculations. Finally, the $CsPbBr_3$:Na NCs were applied as phosphors in WLED applications, and the light emission with a CCT of 6652 K, CRI of 75.2, CIE coordinates of (0.31, 0.33), and power efficiency of 67.3 l m/W was obtained. More importantly, the proposed $CsPbBr_3$:Na NC WLEDs demonstrated a remarkable operation stability in ambient air under the continuous current mode. After a continuous operation for 500 h, only 15% decay can be observed, which shows great superiority to the device with fresh $CsPbBr_3$ NCs as the phosphors. It can be anticipated that this work provides an effective strategy to enhance the emission performance and stability of perovskite NCs.

DOI: 10.1021/acs.chemmater.8b05362
Chem. Mater. 2019, 31, 3917−3928

EXPERIMENTAL SECTION

Materials and Chemicals. Lead(II) bromide ($PbBr_2$, 99.9%) and cesium bromide (CsBr, 99.9%) were purchased from Xi'an Polymer Light Technology Corp. Sodium bromide (NaBr, 99.9%), oleic acid (OA, 99%), oleylamine (OAm, 99%), dimethylformamide (DMF, 99.9%), and toluene were purchased from Alfa Aesar. All the chemicals were used without further purification.

Synthesis of Undoped and Na^+-Doped Orthorhombic $CsPbBr_3$ NCs. In this work, orthorhombic $CsPbBr_3$:Na NCs with different Na/Pb atom ratios were synthesized following the reported solution recrystallization method with some modifications at RT.[23,75,76] As schematically illustrated in Figure 1a, in a typical synthesis, the precursor solution A was prepared by dissolving $PbBr_2$ (0.4 mmol), CsBr (0.4 mmol), OA (1 mL), and OAm (0.5 mL) in DMF (10 mL) under vigorous stirring for 30 min. Further, the precursor solution B was prepared by dissolving NaBr (1 mmol) in DMF (1 mL). Then, 0, 15, 30, 50, and 100 μL of the precursor solution B were mixed with 1 mL of the precursor solution A to form a mixture with Na/Pb = 0, 0.375, 0.75, 1.25, and 2.5, respectively. Next, the mixture was added dropwise into toluene (10 mL) under vigorous stirring to form $CsPbBr_3$:Na NCs. The precipitates including large-sized $CsPbBr_3$:Na particles and the remaining raw materials in the solution were discarded. Finally, the upper uniform liquid was centrifuged at 10 000 rpm to obtain the NCs and then dispersed in toluene for further analysis. Figure 1b displays the optical images of the as-prepared $CsPbBr_3$:Na NC colloidal solution under ambient conditions and UV lamp irradiation, and the intense and uniform green emission suggests the excellent luminescence performance of the $CsPbBr_3$:Na NCs and the absence of the aggregation phenomenon. Finally, five samples with different nominal doping concentrations of 0, 0.375:1, 0.75:1, 1.25:1, and 2.5:1 for Na/Pb ratios were synthesized with the same method, by just changing the amount of NaBr in the precursors.

Fabrication of WLEDs with Orthorhombic $CsPbBr_3$:Na NCs. First, the dried green-emissive $CsPbBr_3$:Na NCs were mixed with the commercial red-emissive $K_2SiF_6:Mn^{4+}$ powder at a certain weight ratio in a polydimethylsiloxane encapsulant (Dow Corning, SYLGARD 184 Silicone Elastomer) to obtain a homogeneous mixture. Then, the mixture was put in a vacuum chamber to get rid of the bubbles inside. At last, the precursor mixture was dropped in the window of the blue-emissive LED (470 nm) and then solidified on a hot plate at 40 °C for 40 min and at 130 °C for 100 min sequentially. Note that all these procedures were carried out in a N_2-filled glovebox.

Characterizations. The crystallinity characteristics of the products were analyzed by XRD (PANalytical X'Pert PRO) with the radiation source of Cu Kα (0.1541 nm). The morphology and microstructure of the as-synthesized NCs were analyzed using a high-resolution TEM (JEM-2100) with an operating voltage of 200 kV, and an EDS detector (Oxford X-Max 65) attached to a transmission electron microscope was utilized to study the chemical compositions of the NCs. The optical absorption spectra of the Na^+-doped $CsPbBr_3$ NCs in toluene were measured with a Shimadzu UV-3600 spectrophotometer at RT. The steady-state PL spectra of the NCs were recorded by a double-grating spectrofluorometer (Horiba; Fluorolog-3) with an excitation wavelength of 370 nm and a bandpass of 1 nm. A fluorescence lifetime measurement system was used to test the time-resolved PL, using a 1.4 ns pulsed LED (Horiba; NanoLED) as the light source, which was operated at 370 nm. For measuring the temperature-dependent PL and temperature-dependent fluorescence lifetime, the spectrofluorometer was equipped with a LakeShore-325 digital temperature controller and a Jannis CCS-100 closed-cycle helium cryostat to provide a temperature variation from 10 to 300 K with an accuracy of 1 K. A fluorescence spectrometer (Horiba; FluoroMax-4) with an integrated sphere (Horiba; Quanta-φ) was used to test the absolute PLQY of the $CsPbBr_3$:Na NC solution. The emission spectra of the WLEDs were recorded by using a Keithley 2400 source and a PR650 SpectraScan spectrophotometer (Photo Research) in air and at RT.

Computational Methods. Our first-principles calculations were based on DFT using the plane wave pseudopotential approach as implemented in the Vienna Ab initio Simulation Package. The electron−ion interactions are described by means of the projected augmented-wave pseudopotentials with $5s^25p^66s$ for Cs, $2s^22p^63s$ for Na, $6s^26p^2$ for Pb, and $4s^24p^5$ for Br as valence electrons. We used the Perdew−Burke−Ernzerhof parameterization of the generalized gradient approximation (GGA) as the exchange correlation functional. Experimental lattice constants of the RT orthorhombic phase $CsPbBr_3$ were used: a = 8.25 Å, b = 8.46 Å, c = 11.91 Å. We simulated the isolated impurities in the 2 × 2 × 1 supercells. A kinetic energy cutoff of 400 eV for wave function expansion and 1 × 1 × 2 reciprocal k-point mesh were used for total energy minimization. It was considered that until the residual forces were less than 0.01 eV/Å, the atomic positions were fully relaxed. For negatively or positively charged impurities, the extra electrons or holes together with uniform compensating charges were added into the supercell. The formation energy ΔH of the impurities was calculated according to the following equation

$$\Delta H = (E_D - E_H) - \sum_i n_i(\mu_i + \mu_i^{bulk}) + q(\varepsilon_{VBM} + \varepsilon_f) + \Delta E_{corr} \quad (6)$$

in which E_D is the energy of the impurity-containing supercells and E_H is the total energy of the impurity-free ones. n_i is the atomic species difference in the number between the defect-free and defect-containing supercells. μ_i is the relative chemical potential of the atomic species with reference to its bulk μ_i^{bulk}, ε_{VBM} is the energy of the host material VBM and ε_f is the Fermi energy relative to the VBM. ΔE_{corr} is the correction to the supercell simulation including potential alignment and image charge correction. The effect of spin−orbital coupling (SOC) was previously reported because of the strong relativistic effect of Pb. However, the band gap errors of using generalized GGA and non-SOC cancel with each other in the orthorhombic $CsPbBr_3$ structure. The GGA non-SOC produces a band gap of 2.13 eV for $CsPbBr_3$, which is in good agreement with the experimental value of 2.25 eV. Therefore, SOC was not considered in our formation energy calculations.

ASSOCIATED CONTENT

Supporting Information

The Supporting Information is available free of charge on the ACS Publications website at DOI: 10.1021/acs.chemmater.8b05362.

Detailed observation of XRD of the NC examples at ~31.0°; XPS spectra of $CsPbBr_3$ and $CsPbBr_3$:Na (Na/Pb = 1.25) NC films; size distribution statistics of $CsPbBr_3$:Na NCs with different Na/Pb ratios; elemental analysis of the NC samples; comparison of the PLQY of the samples with different Na/Pb atom ratios; PL spectra of $CsPbBr_3$:Na NCs after purification; temperature-dependent PL spectra of $CsPbBr_3$ and $CsPbBr_3$:Na NCs; calculation of the nonradiative rate constant of $CsPbBr_3$:Na NCs with the Na/Pb ratios of 0 and 1.25 at RT; temperature-dependent PL spectra of $CsPbBr_3$:Na NCs and $CsPbBr_3$ NCs; stability of $CsPbBr_3$:Na NCs with different Na/Pb ratios; investigation on the PL stability and XRD stability of the $CsPbBr_3$ and $CsPbBr_3$:Na NCs; emission contributions in the $CsPbBr_3$:Na NC WLEDs; WLEDs constructed with fresh $CsPbBr_3$ NCs; and stability of WLEDs constructed with the fresh $CsPbBr_3$ NCs (PDF)

DOI: 10.1021/acs.chemmater.8b05362
Chem. Mater. 2019, 31, 3917−3928

AUTHOR INFORMATION

Corresponding Authors

*E-mail: shizf@zzu.edu.cn (Z.S.).
*E-mail: yangdw@zzu.edu.cn (D.Y.).
*E-mail: lixj@zzu.edu.cn (X.J.L.).

ORCID

Zhifeng Shi: 0000-0002-9416-3948
Di Wu: 0000-0003-3266-0612
Yuantao Zhang: 0000-0002-8671-6979
Xin Jian Li: 0000-0001-5338-7112

Notes

The authors declare no competing financial interest.

ACKNOWLEDGMENTS

This work was supported by the National Natural Science Foundation of China (nos. 11774318, 11604302, 61176044 and 11504331), the China Postdoctoral Science Foundation (2017T100535 and 2018M642766), the Key Scientific Research Projects of Higher Education in Henan Province (18A140007), the Support Program for Scientific and Technological Innovation Talents of Higher Education in Henan Province (19HASTIT017), and the Outstanding Young Talent Research Fund of Zhengzhou University (1521317001).

REFERENCES

(1) Møller, C. K. Crystal Structure and Photoconductivity of Cæsium Plumbohalides. *Nature* **1958**, *182*, 1436.

(2) Hirotsu, S.; Harada, J.; Iizumi, M.; Gesi, K. Structural Phase Transitions in $CsPbBr_3$. *J. Phys. Soc. Jpn.* **1974**, *37*, 1393−1398.

(3) Scaife, D. E.; Weller, P. F.; Fisher, W. G. Crystal preparation and properties of cesium tin(II) trihalides. *J. Solid State Chem.* **1974**, *9*, 308−314.

(4) Weber, D. $CH_3NH_3PbX_3$, ein Pb (II)-System Mit Kubischer Perowskitstruktur/$CH_3NH_3PbX_3$, a Pb (II)-system with Cubic Perovskite Structure. *Z. Naturforsch., B: Anorg. Chem., Org. Chem.* **1978**, *33*, 1443−1445.

(5) Thiele, G.; Rotter, H. W.; Schmidt, K. D. Kristallstrukturen und Phasentransformationen von Caesiumtrihalogenogermanaten(II) CsGeX3 (X = Cl, Br, I). *Z. Anorg. Allg. Chem.* **1987**, *545*, 148−156.

(6) Mitzi, D. B. Thin-Film Deposition of Organic−Inorganic Hybrid Materials. *Chem. Mater.* **2001**, *13*, 3283−3298.

(7) Kojima, A.; Teshima, K.; Shirai, Y.; Miyasaka, T. Organometal Halide Perovskites as Visible-Light Sensitizers for Photovoltaic Cells. *J. Am. Chem. Soc.* **2009**, *131*, 6050−6051.

(8) Kim, H.-S.; Lee, C.-R.; Im, J.-H.; Lee, K.-B.; Moehl, T.; Marchioro, A.; Moon, S.-J.; Humphry-Baker, R.; Yum, J.-H.; Moser, J.E.; Grätzel, M.; Park, N.-G. Lead iodide perovskite sensitized all-solid-state submicron thin film mesoscopic solar cell with efficiency exceeding 9%. *Sci Rep* **2012**, *2*, 591−591.

(9) Lee, M. M.; Teuscher, J.; Miyasaka, T.; Murakami, T. N.; Snaith, H. J. Efficient Hybrid Solar Cells Based on Meso-Superstructured Organometal Halide Perovskites. *Science* **2012**, *338*, 643−647.

(10) Eperon, G. E.; Burlakov, V. M.; Docampo, P.; Goriely, A.; Snaith, H. J. Morphological Control for High Performance, Solution-Processed Planar Heterojunction Perovskite Solar Cells. *Adv. Funct. Mater.* **2014**, *24*, 151−157.

(11) Kulbak, M.; Cahen, D.; Hodes, G. How Important Is the Organic Part of Lead Halide Perovskite Photovoltaic Cells? Efficient $CsPbBr_3$ Cells. *J. Phys. Chem. Lett.* **2015**, *6*, 2452−2456.

(12) Wang, M.; Shi, Y.; Bian, J.; Dong, Q.; Sun, H.; Liu, H.; Luo, Y.; Zhang, Y. Electroluminescence from Perovskite LEDs With the Structure of Ag/Spiro-OMeTAD/$CH_3NH_3PbI_3$/TiO_2/FTO. *Chem. Phys. Lett.* **2016**, *662*, 176−181.

(13) Li, J.; Xu, L.; Wang, T.; Song, J.; Chen, J.; Xue, J.; Dong, Y.; Cai, B.; Shan, Q.; Han, B.; Zeng, H. 50-Fold EQE Improvement up to 6.27% of Solution-Processed All-Inorganic Perovskite $CsPbBr_3$ QLEDs via Surface Ligand Density Control. *Adv. Mater.* **2017**, *29*, 1603885.

(14) Ngo, T. T.; Suarez, I.; Antonicelli, G.; Cortizo-Lacalle, D.; Martinez-Pastor, J. P.; Mateo-Alonso, A.; Mora-Sero, I. Enhancement of the Performance of Perovskite Solar Cells, LEDs, and Optical Amplifiers by Anti-Solvent Additive Deposition. *Adv. Mater.* **2017**, *29*, 1604056.

(15) Shi, Z.; Li, Y.; Zhang, Y.; Chen, Y.; Li, X.; Wu, D.; Xu, T.; Shan, C.; Du, G. High-Efficiency and Air-Stable Perovskite Quantum Dots Light-Emitting Diodes with an All-Inorganic Heterostructure. *Nano Lett.* **2017**, *17*, 313−321.

(16) Ramasamy, P.; Lim, D.-H.; Kim, B.; Lee, S.-H.; Lee, M.-S.; Lee, J.-S. All-Inorganic Cesium Lead Halide Perovskite Nanocrystals for Photodetector Applications. *Chem. Commun.* **2016**, *52*, 2067−2070.

(17) Wei, H.; Fang, Y.; Mulligan, P.; Chuirazzi, W.; Fang, H.-H.; Wang, C.; Ecker, B. R.; Gao, Y.; Loi, M. A.; Cao, L.; Huang, J. Sensitive X-ray Detectors Made of Methylammonium Lead Tribromide Perovskite Single Crystals. *Nat. Photonics* **2016**, *10*, 333−339.

(18) Li, Y.; Shi, Z.-F.; Li, S.; Lei, L.-Z.; Ji, H.-F.; Wu, D.; Xu, T.-T.; Tian, Y.-T.; Li, X.-J. High-Performance Perovskite Photodetectors Based on Solution-Processed All-Inorganic $CsPbBr_3$ Thin Films. *J. Mater. Chem. C* **2017**, *5*, 8355−8360.

(19) Shi, Z.; Li, Y.; Li, S.; Li, X.; Wu, D.; Xu, T.; Tian, Y.; Chen, Y.; Zhang, Y.; Zhang, B.; Shan, C.; Du, G. Localized Surface Plasmon Enhanced All-Inorganic Perovskite Quantum Dot Light-Emitting Diodes Based on Coaxial Core/Shell Heterojunction Architecture. *Adv. Funct. Mater.* **2018**, *28*, 1707031.

(20) Yakunin, S.; Protesescu, L.; Krieg, F.; Bodnarchuk, M. I.; Nedelcu, G.; Humer, M.; De Luca, G.; Fiebig, M.; Heiss, W.; Kovalenko, M. V. Low-Threshold Amplified Spontaneous Emission and Lasing from Colloidal Nanocrystals of Caesium Lead Halide Perovskites. *Nat. Commun.* **2015**, *6*, 8056.

(21) Li, G.; Price, M.; Deschler, F. Research Update: Challenges for high-efficiency hybrid lead-halide perovskite LEDs and the path towards electrically pumped lasing. *APL Mater.* **2016**, *4*, 091507.

(22) Saliba, M.; Wood, S. M.; Patel, J. B.; Nayak, P. K.; Huang, J.; Alexander-Webber, J. A.; Wenger, B.; Stranks, S. D.; Hörantner, M. T.; Wang, J. T.-W.; Nicholas, R. J.; Herz, L. M.; Johnston, M. B.; Morris, S. M.; Snaith, H. J.; Riede, M. K. Structured Organic-Inorganic Perovskite toward a Distributed Feedback Laser. *Adv. Mater.* **2016**, *28*, 923−929.

(23) Li, X.; Wu, Y.; Zhang, S.; Cai, B.; Gu, Y.; Song, J.; Zeng, H. $CsPbX_3$ Quantum Dots for Lighting and Displays: Room-Temperature Synthesis, Photoluminescence Superiorities, Underlying Origins and White Light-Emitting Diodes. *Adv. Funct. Mater.* **2016**, *26*, 2435−2445.

(24) Mondal, N.; De, A.; Samanta, A. Achieving Near-Unity Photoluminescence Efficiency for Blue-violet Emitting Perovskite Nanocrystals. *ACS Energy Lett.* **2019**, *4*, 32−39.

(25) Protesescu, L.; Yakunin, S.; Bodnarchuk, M. I.; Krieg, F.; Caputo, R.; Hendon, C. H.; Yang, R. X.; Walsh, A.; Kovalenko, M. V. Nanocrystals of Cesium Lead Halide Perovskites ($CsPbX_3$, X = Cl, Br, and I): Novel Optoelectronic Materials Showing Bright Emission with Wide Color Gamut. *Nano Lett.* **2015**, *15*, 3692−3696.

(26) Huang, H.; Susha, A. S.; Kershaw, S. V.; Hung, T. F.; Rogach, A. L. Control of Emission Color of High Quantum Yield $CH_3NH_3PbBr_3$ Perovskite Quantum Dots by Precipitation Temperature. *Adv. Sci.* **2015**, *2*, 1500194.

(27) Shi, Z. F.; Li, S.; Li, Y.; Ji, H. F.; Li, X. J.; Wu, D.; Xu, T. T.; Chen, Y. S.; Tian, Y. T.; Zhang, Y. T.; Shan, C. X.; Du, G. T. Strategy of Solution-Processed All-Inorganic Heterostructure for Humidity/Temperature-Stable Perovskite Quantum Dot Light-Emitting Diodes. *ACS Nano* **2018**, *12*, 1462−1472.

(28) Protesescu, L.; Yakunin, S.; Bodnarchuk, M. I.; Bertolotti, F.; Masciocchi, N.; Guagliardi, A.; Kovalenko, M. V. Monodisperse

DOI: 10.1021/acs.chemmater.8b05362
Chem. Mater. 2019, 31, 3917−3928

Formamidinium Lead Bromide Nanocrystals with Bright and Stable Green Photoluminescence. *J. Am. Chem. Soc.* **2016**, *138*, 14202−14205.
(29) Meyns, M.; Perálvarez, M.; Heuer-Jungemann, A.; Hertog, W.; Ibáñez, M.; Nafria, R.; Genç, A.; Arbiol, J.; Kovalenko, M. V.; Carreras, J.; Cabot, A.; Kanaras, A. G. Polymer-Enhanced Stability of Inorganic Perovskite Nanocrystals and Their Application in Color Conversion LEDs. *ACS Appl. Mater. Interfaces* **2016**, *8*, 19579−19586.
(30) Palazon, F.; Di Stasio, F.; Akkerman, Q. A.; Krahne, R.; Prato, M.; Manna, L. Polymer-Free Films of Inorganic Halide Perovskite Nanocrystals as UV-to-White Color-Conversion Layers in LEDs. *Chem. Mater.* **2016**, *28*, 2902−2906.
(31) Dursun, I.; Shen, C.; Parida, M. R.; Pan, J.; Sarmah, S. P.; Priante, D.; Alyami, N.; Liu, J.; Saidaminov, M. I.; Alias, M. S.; Abdelhady, A. L.; Ng, T. K.; Mohammed, O. F.; Ooi, B. S.; Bakr, O. M. Perovskite Nanocrystals as a Color Converter for Visible Light Communication. *ACS Photonics* **2016**, *3*, 1150−1156.
(32) Zhou, Q.; Bai, Z.; Lu, W.-g.; Wang, Y.; Zou, B.; Zhong, H. In Situ Fabrication of Halide Perovskite Nanocrystal-Embedded Polymer Composite Films with Enhanced Photoluminescence for Display Backlights. *Adv. Mater.* **2016**, *28*, 9163−9168.
(33) Yoon, H. C.; Kang, H.; Lee, S.; Oh, J. H.; Yang, H.; Do, Y. R. Study of Perovskite QD Down-Converted LEDs and Six-Color White LEDs for Future Displays with Excellent Color Performance. *ACS Appl. Mater. Interfaces* **2016**, *8*, 18189−18200.
(34) Kulbak, M.; Gupta, S.; Kedem, N.; Levine, I.; Bendikov, T.; Hodes, G.; Cahen, D. Cesium Enhances Long-Term Stability of Lead Bromide Perovskite-Based Solar Cells. *J. Phys. Chem. Lett.* **2016**, *7*, 167−172.
(35) Huang, S.; Li, Z.; Kong, L.; Zhu, N.; Shan, A.; Li, L. Enhancing the Stability of $CH_3NH_3PbBr_3$ Quantum Dots by Embedding in Silica Spheres Derived from Tetramethyl Orthosilicate in "Waterless" Toluene. *J. Am. Chem. Soc.* **2016**, *138*, 5749−5752.
(36) Cho, H.; Kim, Y.-H.; Wolf, C.; Lee, H.-D.; Lee, T.-W. Improving the Stability of Metal Halide Perovskite Materials and Light-Emitting Diodes. *Adv. Mater.* **2018**, *30*, 1704587.
(37) Yuan, Y.; Huang, J. Ion Migration in Organometal Trihalide Perovskite and Its Impact on Photovoltaic Efficiency and Stability. *Acc. Chem. Res.* **2016**, *49*, 286−293.
(38) Niu, G.; Guo, X.; Wang, L. Review of Recent Progress in Chemical Stability of Perovskite Solar Cells. *J. Mater. Chem. A* **2015**, *3*, 8970−8980.
(39) Leijtens, T.; Eperon, G. E.; Noel, N. K.; Habisreutinger, S. N.; Petrozza, A.; Snaith, H. J. Stability of Metal Halide Perovskite Solar Cells. *Adv. Energy Mater.* **2015**, *5*, 1500963.
(40) Wang, Q.; Lyu, M.; Zhang, M.; Yun, J.-H.; Chen, H.; Wang, L. Transition From the Tetragonal to Cubic Phase of Organohalide Perovskite: The Role of Chlorine in Crystal Formation of $CH_3NH_3PbI_3$ on TiO_2 Substrates. *J. Phys. Chem. Lett.* **2015**, *6*, 4379−4384.
(41) Ji, L.; Li, W.; Xi, Y.; Bo, B.; Li, H.; Zhao, J.; Gao, X. Ultraviolet Light Induced Degradation of Luminescence in $CsPbBr_3$ Perovskite Nanocrystals. *Mater. Res. Bull.* **2018**, *102*, 86−91.
(42) Huang, H.; Bodnarchuk, M. I.; Kershaw, S. V.; Kovalenko, M. V.; Rogach, A. L. Lead Halide Perovskite Nanocrystals in the Research Spotlight: Stability and Defect Tolerance. *ACS Energy Lett.* **2017**, *2*, 2071−2083.
(43) Xu, L.; Chen, J.; Song, J.; Li, J.; Xue, J.; Dong, Y.; Cai, B.; Shan, Q.; Han, B.; Zeng, H. Double-Protected All-Inorganic Perovskite Nanocrystals by Crystalline Matrix and Silica for Triple-Modal Anti-Counterfeiting Codes. *ACS Appl. Mater. Interfaces* **2017**, *9*, 26556−26564.
(44) Sun, C.; Zhang, Y.; Ruan, C.; Yin, C.; Wang, X.; Wang, Y.; Yu, W. W. Efficient and Stable White LEDs with Silica-Coated Inorganic Perovskite Quantum Dots. *Adv. Mater.* **2016**, *28*, 10088−10094.
(45) Li, Z.; Kong, L.; Huang, S.; Li, L. Highly Luminescent and Ultra-Stable $CsPbBr_3$ Pervoskite Quantum Dots-Silica/Alumina Monolith. *Angew. Chem.* **2017**, *129*, 8246−8250.
(46) Zhang, F.; Shi, Z.-F.; Ma, Z.-Z.; Li, Y.; Li, S.; Wu, D.; Xu, T.-T.; Li, X.-J.; Shan, C.-X.; Du, G.-T. Silica Coating Enhances the Stability of Inorganic Perovskite Nanocrystals for Efficient and Stable Down-Conversion in White Light-Emitting Devices. *Nanoscale* **2018**, *10*, 20131−20139.
(47) Song, E.; Ding, S.; Wu, M.; Ye, S.; Xiao, F.; Zhou, S.; Zhang, Q. Anomalous NIR Luminescence in Mn^{2+}-Doped Fluoride Perovskite Nanocrystals. *Adv. Opt. Mater.* **2014**, *2*, 670−678.
(48) Begum, R.; Parida, M. R.; Abdelhady, A. L.; Murali, B.; Alyami, N. M.; Ahmed, G. H.; Hedhili, M. N.; Bakr, O. M.; Mohammed, O. F. Engineering Interfacial Charge Transfer in $CsPbBr_3$ Perovskite Nanocrystals by Heterovalent Doping. *J. Am. Chem. Soc.* **2017**, *139*, 731−737.
(49) Huang, G.; Wang, C.; Xu, S.; Zong, S.; Lu, J.; Wang, Z.; Lu, C.; Cui, Y. Postsynthetic Doping of $MnCl_2$ Molecules into Preformed $CsPbBr_3$ Perovskite Nanocrystals *via* a Halide Exchange-Driven Cation Exchange. *Adv. Mater.* **2017**, *29*, 1700095.
(50) Li, X.; Zhong, X.; Hu, Y.; Li, B.; Sheng, Y.; Zhang, Y.; Weng, C.; Feng, M.; Han, H.; Wang, J. Organic-Inorganic Copper(II)-Based Material: A Low-Toxic, Highly Stable Light Absorber for Photovoltaic Application. *J. Phys. Chem. Lett.* **2017**, *8*, 1804−1809.
(51) Lin, C. C.; Xu, K. Y.; Wang, D.; Meijerink, A. Luminescent Manganese-Doped $CsPbCl_3$ Perovskite Quantum Dots. *Sci. Rep.* **2017**, *7*, 45906.
(52) Liu, M.; Zhong, G.; Yin, Y.; Miao, J.; Li, K.; Wang, C.; Xu, X.; Shen, C.; Meng, H. Aluminum-Doped Cesium Lead Bromide Perovskite Nanocrystals with Stable Blue Photoluminescence Used for Display Backlight. *Adv. Sci.* **2017**, *4*, 1700335.
(53) Miao, X.; Qiu, T.; Zhang, S.; Ma, H.; Hu, Y.; Bai, F.; Wu, Z. Air-Stable $CsPb_{1-x}Bi_xBr_3$ ($0 \leq x \leq 1$) Perovskite Crystals: Optoelectronic and Photostriction Properties. *J. Mater. Chem. C* **2017**, *5*, 4931−4939.
(54) Stam, W. v. d.; Geuchies, J. J.; Altantzis, T.; Bos, K. H. V. D.; Meeldijk, J. D.; Aert, S. V.; Bals, S.; Vanmaekelbergh, D.; Donega, C. D. M. Highly Emissive Divalent-Ion-Doped Colloidal $CsPb_{1-x}M_xBr_3$ Perovskite Nanocrystals through Cation Exchange. *J. Am. Chem. Soc.* **2017**, *139*, 4087−4097.
(55) Wang, H.-C.; Wang, W.; Tang, A.-C.; Tsai, H.-Y.; Bao, Z.; Ihara, T.; Yarita, N.; Tahara, H.; Kanemitsu, Y.; Chen, S.; Liu, R.-S. -Performance $CsPb_{1-x}Sn_xBr_3$ Perovskite Quantum Dots for Light-Emitting Diodes. *Angew. Chem., Int. Ed.* **2017**, *56*, 13650−13654.
(56) Zhou, Y.; Chen, J.; Bakr, O. M.; Sun, H.-T. Metal-Doped Lead Halide Perovskites: Synthesis, Properties, and Optoelectronic Applications. *Chem. Mater.* **2018**, *30*, 6589−6613.
(57) Liu, Y.; Pan, G.; Wang, R.; Shao, H.; Wang, H.; Xu, W.; Cui, H.; Song, H. Considerably Enhanced Exciton Emission of $CsPbCl_3$ Perovskite Quantum Dots by the Introduction of Potassium and Lanthanide Ions. *Nanoscale* **2018**, *10*, 14067−14072.
(58) Pan, G.; Bai, X.; Yang, D.; Chen, X.; Jing, P.; Qu, S.; Zhang, L.; Zhou, D.; Zhu, J.; Xu, W.; Dong, B.; Song, H. Doping Lanthanide into Perovskite Nanocrystals: Highly Improved and Expanded Optical Properties. *Nano Lett.* **2017**, *17*, 8005−8011.
(59) Hu, Q.; Li, Z.; Tan, Z.; Song, H.; Ge, C.; Niu, G.; Han, J.; Tang, J. Rare Earth Ion-Doped $CsPbBr_3$ Nanocrystals. *Adv. Opt. Mater.* **2018**, *6*, 1700864.
(60) Li, F.; Xia, Z.; Gong, Y.; Gu, L.; Liu, Q. Optical Properties of Mn^{2+} doped Cesium Lead Halide Perovskite Nanocrystals *via* a Cation-Anion Cosubstitution Exchange Reaction. *J. Mater. Chem. C* **2017**, *5*, 9281−9287.
(61) Zhao, W.; Yao, Z.; Yu, F.; Yang, D.; Liu, S. F. Alkali Metal Doping for Improved $CH_3NH_3PbI_3$ Perovskite Solar Cells. *Adv. Sci.* **2018**, *5*, 1700131.
(62) Cao, J.; Tao, S. X.; Bobbert, P. A.; Wong, C.-P.; Zhao, N. Interstitial Occupancy by Extrinsic Alkali Cations in Perovskites and Its Impact on Ion Migration. *Adv. Mater.* **2018**, *30*, 1707350.
(63) Son, D.-Y.; Kim, S.-G.; Seo, J.-Y.; Lee, S.-H.; Shin, H.; Lee, D.; Park, N.-G. Universal Approach toward Hysteresis-Free Perovskite Solar Cell *via* Defect Engineering. *J. Am. Chem. Soc.* **2018**, *140*, 1358−1364.

DOI: 10.1021/acs.chemmater.8b05362
Chem. Mater. 2019, 31, 3917−3928

(64) Li, Y.; Duan, J.; Yuan, H.; Zhao, Y.; He, B.; Tang, Q. Lattice Modulation of Alkali Metal Cations Doped $Cs_{1-x}R_xPbBr_3$ Halides for Inorganic Perovskite Solar Cells. *Sol. RRL* **2018**, *2*, 1800164.
(65) Sakuma, T.; Mutou, M.; Ohki, K.; Arai, M.; Takahashi, H.; Ishii, Y. Low-Energy Excitation in $CsPbX_3$ (X= Cl, Br). *Solid State Ionics* **2002**, *154*−*155*, 237−242.
(66) Yang, Y.; Yang, M.; Li, Z.; Crisp, R.; Zhu, K.; Beard, M. C. Comparison of Recombination Dynamics in $CH_3NH_3PbBr_3$ and $CH_3NH_3PbI_3$ Perovskite Films: Influence of Exciton Binding Energy. *J. Phys. Chem. Lett.* **2015**, *6*, 4688−4692.
(67) Wang, Q.; Liu, X.-D.; Qiu, Y.-H.; Chen, K.; Zhou, L.; Wang, Q.-Q. Quantum Confinement Effect and Exciton Binding Energy of Layered Perovskite Nanoplatelets. *AIP Adv.* **2018**, *8*, 025108.
(68) Droseros, N.; Longo, G.; Brauer, J. C.; Sessolo, M.; Bolink, H. J.; Banerji, N. Origin of the Enhanced Photoluminescence Quantum Yield in $MAPbBr_3$ Perovskite with Reduced Crystal Size. *ACS Energy Lett.* **2018**, *3*, 1458−1466.
(69) Dey, P.; Paul, J.; Bylsma, J.; Karaiskaj, D.; Luther, J. M.; Beard, M. C.; Romero, A. H. Origin of the Temperature Dependence of the Band Gap of PbS and PbSe Quantum Dots. *Solid State Commun.* **2013**, *165*, 49−54.
(70) Xing, J.; Liu, X. F.; Zhang, Q.; Ha, S. T.; Yuan, Y. W.; Shen, C.; Sum, T. C.; Xiong, Q. Vapor Phase Synthesis of Organometal Halide Perovskite Nanowires for Tunable Room-Temperature Nanolasers. *Nano Lett.* **2015**, *15*, 4571−4577.
(71) Ming, W.; Chen, S.; Du, M.-H. Chemical Instability Leads to Unusual Chemical-Potential-Independent Defect Formation and Diffusion in Perovskite Solar Cell Material $CH_3NH_3PbI_3$. *J. Mater. Chem. A* **2016**, *4*, 16975−16981.
(72) Yin, W.-J.; Shi, T.; Yan, Y. Unusual Defect Physics in $CH_3NH_3PbI_3$ Perovskite Solar Cell Absorber. *Appl. Phys. Lett.* **2014**, *104*, 063903.
(73) Carrillo-Carrión, C.; Cárdenas, S.; Simonet, B. M.; Valcárcel, M. Quantum Dots Luminescence Enhancement Due to Illumination with UV/Vis Light. *Chem. Commun.* **2009**, 5214−5226.
(74) Chen, J.; Liu, D.; Al-Marri, M. J.; Nuuttila, L.; Lehtivuori, H.; Zheng, K. Photo-Stability of $CsPbBr_3$ Perovskite Quantum Dots for Optoelectronic Application. *Sci. China Mater.* **2016**, *59*, 719−727.
(75) Zhu, J.; Yang, X.; Zhu, Y.; Wang, Y.; Cai, J.; Shen, J.; Sun, L.; Li, C. Room-Temperature Synthesis of Mn-Doped Cesium Lead Halide Quantum Dots with High Mn Substitution Ratio. *J. Phys. Chem. Lett.* **2017**, *8*, 4167−4171.
(76) Arunkumar, P.; Gil, K. H.; Won, S.; Unithrattil, S.; Kim, Y. H.; Kim, H. J.; Im, W. B. Colloidal Organolead Halide Perovskite with a High Mn Solubility Limit: A Step Toward Pb-Free Luminescent Quantum Dots. *J. Phys. Chem. Lett.* **2017**, *8*, 4161−4166.

DOI: 10.1021/acs.chemmater.8b05362
Chem. Mater. 2019, 31, 3917−3928